NTNU
Norwegian University of
Science and Technology

What causes the mid-winter cooling?

Frauke Ruth Lotte Fritsch

MSc in Physics
Submission date: May 2016
Supervisor: Patrick Joseph Espy, IFY

Norwegian University of Science and Technology
Department of Physics

Acknowledgement

I want to thank Prof. Patrick J. Espy, who was my supervisor of this master's project. He advised me in terms of background physics, methods, interpretation and scientific writing. I want to thank him for taking the time to answer my questions, both when he was available at NTNU or via email and Skype.

Thanks to Dr. Nora Stray for all the helpful answers and advice, both for the scientific work and the writing process afterwards.

I also want to thank Dr. Rosmarie de Wit for the helpful input and the feedback on the research.

Thanks to Christoph Franzen for all of his support and sense of humor whenever needed.

Summary

This thesis investigated the influence and conditions of vertical propagation of planetary waves on the mid-winter cooling in the southern hemispheric polar mesosphere. MERRA zonal wind data was used to extract planetary waves with zonal wavenumber 1, 2 and 3 at 72° S in 2008 and 2009. The wave periods of 4, 5, 10 and 16 days were separated using Morlet wavelet analysis.

A correlation between the wave amplitude and carbon monoxide as a tracer for vertical motion could be found from autumn until late winter (from March until late August/mid September). Between the wave amplitude and the mean zonal wind anticorrelation was shown from early winter until late winter (April until late August/mid September). Both correlations were found to stop when the mesospheric circulation restores in September. In addition agreement between calculations for the upper bound of the Charney-Drazin criterion for vertical propagation and the wave activity was found until late August/mid September.

Contents

Chapter 1

Introduction

During winter, the temperature and pressure gradients established by the variation of solar heating with latitude, coupled with the Coriolis force, cause strong eastward zonal winds near 40 km. However, gravity, tidal, and planetary waves propagating upward can deposit westward momentum as they become unstable and "break" above 40 km. This westward momentum drives the atmosphere away from a state of radiative equilibrium and establishes a poleward flow in the winter hemisphere. The resulting convergence and downward motion causes adiabatic heating and a warming of the winter pole near 87 km.

However, it is well documented that towards mid-winter the warming and down welling slow in the southern hemisphere (e.g. Gardner et al. [2011], French et al. [2005]). As an example H_2O climatology data in the southern hemisphere indicating vertical motion is shown in figure 1.1.

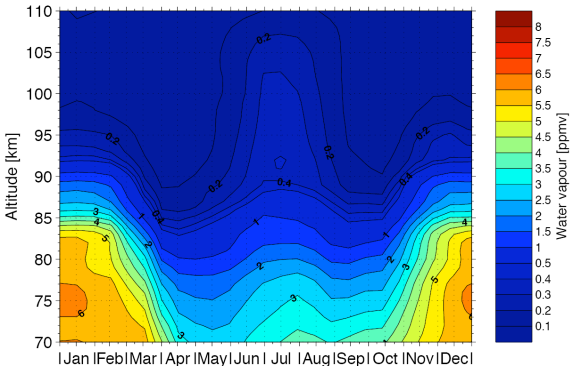

Figure 1.1: Climatology of the southern hermisphere H_2O as a tracer for vertical motion. The increase in vmr in mid-winter indicates slower downward/upward vertical motion [Espy, 2016].

Since the source of H_2O is in the lower atmosphere, its mixing ratio drops with

altitude. In autumn, a line of constant mixing ratio may be seen in figure 1.1 to descend in altitude indicating downward motion of the air. However, during the Austral mid-winter the downward motion ceases and the lines of constant mixing ratio turn around and move upward.

A theoretical study conducted by Plumb [1989] suggests that weak planetary wave activity does not disrupt the wind field at lower altitudes and allows the westward wave momentum to reach the upper atmosphere. Weak planetary wave activity is typical of the southern hemisphere winter. However, this weak planetary wave activity allows the eastward wind to become so strong by mid-winter that the planetary waves are reflected back downward, interrupting the flow of westward momentum to the upper atmosphere and allowing it to relax towards radiative equilibrium (figure 1.2). This strong-wind limit is called the upper bound of the Carney-Drazin Criterion (Charney and Drazin [1961]). On the other hand, the strong planetary wave activity typical of the northern hemisphere can weaken the eastward winds, preventing them from becoming so strong so as to reach this upper bound.

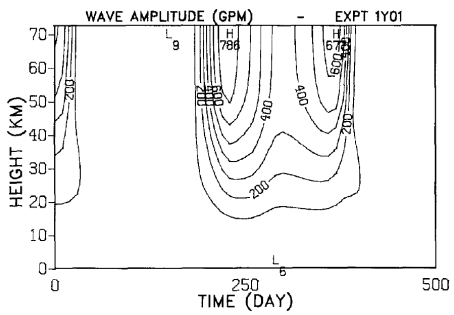

(a) For weak forcing, i.e. forcing amplitude 1 m

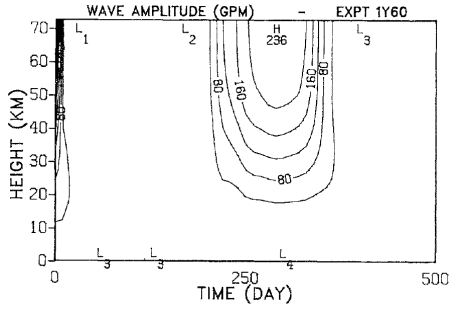

(b) For strong forcing, i.e. forcing amplitude 60 m

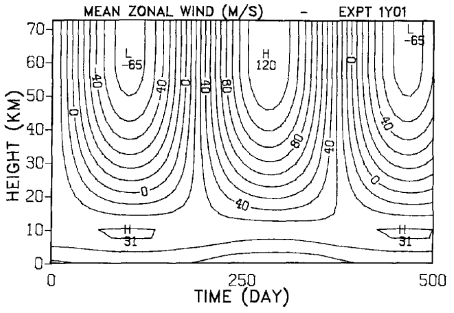

(c) Mean zonal wind for weak forcing

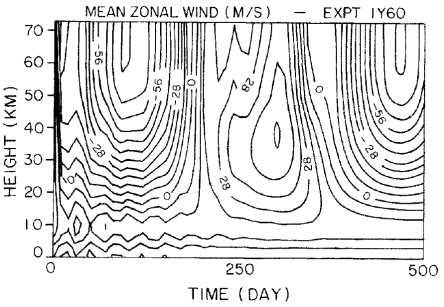

(d) Mean zonal wind for strong forcing

Figure 1.2: Time-height plot of wave amplitude (units 0.1 m geopotential height) and mean zonal wind for weak and strong forcing. From Plumb [1989]

Based on these findings we will investigate the relationship between the plane-

tary wave's strength in the southern hemisphere and the mid winter cooling using measurement driven data.

By gaining more thorough understanding of the vertical motion, better understanding of the transport of ozone depleting species created in the upper atmosphere, for example nitric oxides (NO_X), into the stratospheric ozone layer is possible.

Chapter 2

Background for the problem

2.1 The Atmosphere

To give a better understanding of the problem some further background information is provided in this chapter. General information is based on Andrews [2010], Salby [1996] and Brasseur and Solomon [2005].

Atmospheric layers can be defined by the sign of the temperature gradient. In the troposphere up to about 15 km altitude short-wavelength heating from the sun warms the ground that subsequently transfers its heat to the atmosphere and therefore the temperature decreases with altitude. That is, the temperature gradient is negative. Above that up to about 50 km the gradient is positive mainly due to heating from O_3 that absorbs UV radiation. In the mesosphere from about 50 km to 90 km the predominant radiative cooling from CO_2 leads to a negative temperature gradient. These regions form the lower and middle atmosphere. Within this altitude range the chemical species can be treated as well mixed. The major constituents N_2 ($\sim 80\%$) and O_2 ($\sim 20\%$) are quite stable and rarely react chemically. Above the middle atmosphere, the temperature starts to increase again in the thermosphere due to the dissociation of N_2 and O_2. In this region, the low densities mean that the atmosphere is no longer well mixed and is in diffusive equilibrium.

2.2 Atmospheric dynamics

The atmospheric behavior is determined by radiative, chemical and dynamic processes. The sun drives the atmosphere towards radiative equilibrium whereas dynamics force the atmosphere towards an energetically lower barotropic state. Furthermore, other effects such as the earth's rotation and wave phenomena also influence the general picture. The interplay of those effects results in the observed complex structure. For general descriptions zonal time averages are used to eliminate periodic perturbations.

Thermal winds

Atmospheric temperature gradients, that can for example originate from differences in incoming radiation, give rise to winds. Schematically this is explained for the horizontal case in figure 2.1.

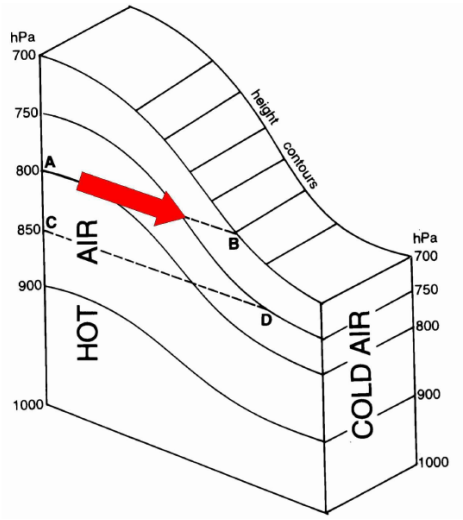

Figure 2.1: Schematic illustration for a temperature gradient which causes a pressure gradient which gives rise to thermal wind. From Geerts and Linacre [2016]

Warm air is less dense than cold air which can be seen from the ideal gas law where $\rho = {}^{p}/_{(R \cdot T)}$. Therefore the pressure is higher in warm places than cold ones at the same altitude. The corresponding pressure gradient causes a wind blowing from warm to cold areas.

When the thermal wind scales are large, the Coriolis force will cause the winds to deflect toward the left (southern hemisphere) or the right (northern hemisphere). For these large scales, the pressure gradient force is balanced by the Coriolis force, and the air will flow along lines of constant pressure perpendicular to the temperature gradient. Under these conditions, the thermal wind is said to be in geostrophic balance.

Gravity waves

Gravity waves (GW) are one type of propagating disturbances in the steady wind field with wavelengths 10 -1,000 km. They originate from vertical displacement of air, e.g. from wind blowing over mountain ranges or convective storms. The required restoring force is the buoyancy force. As air in one layer is displaced upward or downward, a pressure disturbance is created in neighboring layers, which is a longitudinal wave.

The upward wave propagation in the atmosphere depends on the wave's phase speed. Waves begin to become absorbed as their phase speed c approaches the mean zonal wind speed $\bar{u}$. As the zonal wind changes with altitude the waves with different phase speeds are absorbed at different altitude levels. The impact on the background wind is relatively small if the wave is absorbed in the lower atmosphere because the density is still relatively high and the given momentum displaces a large mass. How waves reaching the upper atmosphere are filtered by the low level winds is illustrated in figure 2.2.

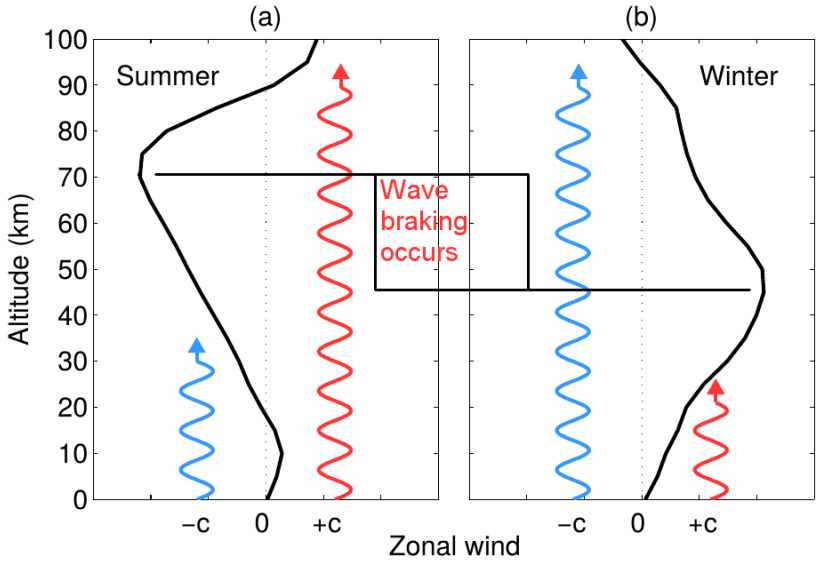

Figure 2.2: Illustration of GW filtering. Zonal wind profiles (black line) at 60° for (a) summer and (b) winter. Blue lines are westward ($c < 0$) GWs and red lines are eastward ($c > 0$) GWs. Taken from de Wit [2015]. The profiles were based on CIRA-86 data.

The zonal wind profiles changing with altitude are shown for winter and summer. The sketch relates GW actitvity to that. As a result of the direction of the radiatively driven winds in the stratosphere, one finds predominantly eastward GWs in summer and westwards GWs in winter higher in the atmosphere. As the density decreases with height the wave amplitude grows due to conservation of energy. At these higher levels the GWs become convectively unstable since the temperature perturbation exceeds the adiabatic lapse rate. Therefore the wave breaks and deposits momentum. The deposited momentum is in the opposite sense to the radiatively driven winds, and therefore slows and turns the background wind. Since the density is low the momentum is sufficient for this effect. If neither of the two aforementioned mechanisms occurs, the waves can dissipate high up in the thermosphere [Fuller-Rowell, 1995].

Planetary waves

Planetary waves (PWs) are large scale waves that span the earth. Their origin is explained by conservation of absolute vorticity in a non-divergent flow. Conservation of vorticity is equivalent to conservation of angular momentum. Absolute vorticity is the sum of the relative vorticity of a parcel of air with respect to surrounding air parcels and the planetary vorticity that occurs because the parcels are rotating about the earth's axis. The planetary vorticity is typically represented by the Coriolis parameter $f = 2\Omega \sin(\phi)$, where Ω is the earth's rotation and ϕ is the latitude. As a parcel of air changes latitude, the planetary vorticity changes and thereby the parcel's relative vorticity has to change respectively. Accordingly it will start to spin clockwise if displaced to the north or opposite if shifted to the south. This is illustrated in figure 2.3.

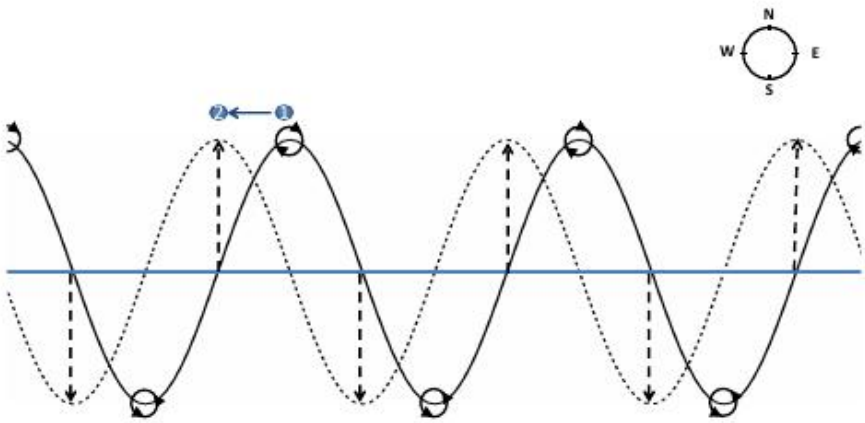

Figure 2.3: Sketch of a planetary wave. The blue line shows the initial equilibrium position of the parcel. The sine waves display the propagation of the wave. The solid line comes before the dashed one in time. Taken from Stray [2015].

As the parcel rotates, it displaces the adjacent parcels. Those west of the initial northward disturbance are forced northwards, where they begin to spin clockwise, while those to the east are forced southwards. That results in a westward propagation of the wave. Planetary waves tend to be stronger in the northern hemisphere as stronger orographic features and land-sea interfaces are found that cause displacement of the airflow and force the waves.

The most common planetary wave periods are given in table 2.1. The third column refers to the type of solution.

The propagation of planetary waves is confined by the background flow. To understand the limits one can start by looking at the wave equation for planetary

Period	Zonal wavenumber	Additional Description
5-day	1	Planetary; first symmetric
10-day	1	Planetray; first asymmetric
16-day	1	Planetary; second symmetric
4-day	2	Planetray; first symmetric
2-day	3	Mixed Planetary-Gravity; asymmetric

Table 2.1: Common planetary waves from Forbes [1995].

waves which is given as:

$$\frac{D}{Dt}\nabla^2\psi' + \beta\frac{\partial\psi'}{\partial x} = 0 \quad \text{with} \quad \beta = \frac{2\Omega\cos\phi_0}{a}.$$

Here ψ' is the geostrophic stream function, ϕ_0 is the initial latitude used in the β-plane approximation and a is the earth's radius. In three dimensions the linearized form of the conservation of vorticity gives the following wave equation:

$$\frac{D}{Dt}\left[\nabla^2\psi' + \left(\frac{f_0^2}{N^2}\right)\frac{1}{\bar{\rho}}\frac{\partial}{\partial z}\left(\bar{\rho}\frac{\partial\psi'}{\partial z}\right)\right] + \beta\frac{\partial\psi'}{\partial x} = 0.$$

Using $f_0 = 2\Omega\sin\phi_0$. $N^2 = \frac{\kappa g}{H}$, where κ is the ratio of the specific gas constant to the specific heat at constant pressure $= \frac{R}{C_p} \approx \frac{2}{7}$, H is the scale height and g is the gravity acceleration. Assuming an exponential solution which increases with hight for the wave equation, one can obtain the following dispersion relation:

$$c - \bar{u} = -\frac{\beta}{k^2 + l^2 + \left(\frac{f_0^2}{N^2}\right)(m^2 + \frac{1}{4H^2})}$$

As β by definition has to be positive and m has to be positive for vertical propagation, the propagation limits are found to be:

$$c < \bar{u} < U_c = \frac{2\Omega\cos(\phi_0)}{a\left(k^2 + l^2 + \frac{(2\Omega\sin(\phi_0))^2}{4\kappa g H}\right)} + c \tag{2.1}$$

whereat U_c denotes to the critical velocity. For $c = 0$, this equation is a representation of the Charney-Drazin criterion [Charney and Drazin, 1961]. Thus waves propagate in flows that are eastward relative to their motion that are not to strong. Accordingly the background wind can form wave guides that also influence the upward propagation of the waves. The upper limit for PW propagation is of particular concern to us, as it illustrates the assumption that planetary waves are blocked by strong eastward winds at low altitudes in the southern winter. A schematic of the resulting waveguides is given in figure 2.4 from Dickinson [1968]. It can be seen that as the waves are confined they propagate through regimes of moderate eastward

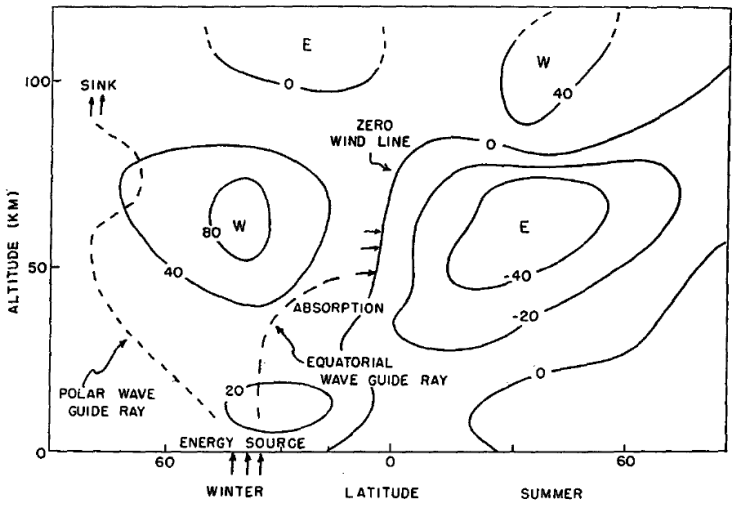

Figure 2.4: Schematic of propagation paths for stationary planetary waves exited in mid-latitude northern hemisphere. W is westerly (eastward), E is easterly (westward). From Dickinson [1968].

(westerly) wind, but are either absorbed or reflected where winds are westward (easterly) or strongly eastward (westerly).

As shown in figure 2.4 the polar wave guides extend to the mesosphere during winter, allowing substantial amounts of westward planetary wave momentum to reach these altitudes. When this momentum is deposited by wave breaking, it supplements the westward momentum deposited by gravity waves.

The faster the wave the lower the upper limit as the wave's phase velocity is westward, i.e. negative. If the wave encounters regimes where $\bar{u} = c$, it breaks and deposits momentum. As planetary waves encounter regions of $\bar{u} > U_c$ they get reflected. Given that this depends on the phase velocity, slower and faster waves can be confined within different latitudes or altitudes. Values for critical velocities for different wave numbers and periods are given in table 4.2 in chapter 4.

However, the fundamental approach in Charney and Drazin [1961] tends to underestimate the value for the critical velocity. More advanced models give a better understanding of how the waveguides can extend to high latitudes in the mesosphere as seen in figure 2.4. An ageostrophic term is included in the approach described in Matsuno [1970] and Andrews et al. [1987]. The resulting equation for the critical velocity for stationary waves is:

$$U_c = \left(2\Omega\cos(\phi) - \frac{1}{a}\left[\frac{(\bar{u}\cos(\phi))_\phi}{\cos(\phi)}\right]_\phi - \frac{af^2}{\rho N^2}\left(\rho\bar{u}_z\right)_z \right) \frac{1}{a\left(k^2 + l^2 + \frac{(2\Omega\sin(\phi))^2}{4\kappa g H}\right)} \tag{2.2}$$

The subscript indices ϕ and z denote to the partial differentiations. f and N^2 were

assumed constant, as we are focusing on one latitude and vertical propagation. Formula 2.2 can be implemented numerically to calculate the differentiations.

2.3 Global circulation

Figure 2.5 shows the global circulation derived from WACCM (Whole Atmosphere Community Climate Model) model data. The most relevant aspects for our question will be explained.

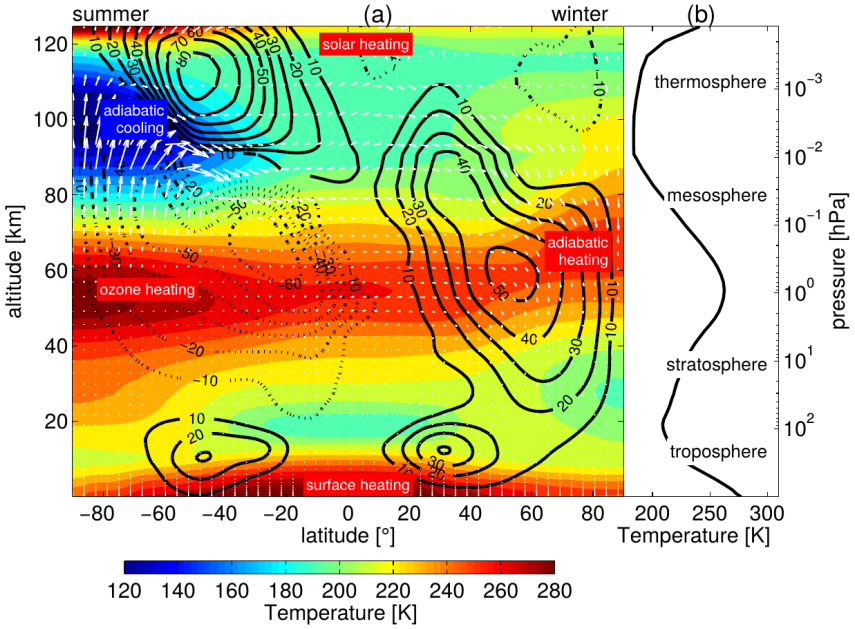

Figure 2.5: Atmospheric structure derived from WACCM. (a) Solstitial atmospheric conditions of zonal-mean temperature (color plot), zonal-mean zonal wind (black contour lines) and zonal-mean vertical and meridional wind (white arrows). The vertical speed has been enlarged for better visibility. (b) Annual-mean temperature structure. Taken from Stray [2015].

Stratospheric mean winds and polar vortex

The stratospheric structure is dominated by radiative equilibrium. As the stratosphere is heated by ozone, it presents a pole-to-pole temperature gradient according to daily insolation. The winter pole is cold and the summer pole is warm. As geostrophic equilibrium can be considered this temperature gradient results in a westward jet in the summer hemisphere and an eastward jet in the winter hemisphere. The eastward jet around the winter pole forms the polar vortex.

Solstitial mesospheric circulation

In the mesosphere gravity waves propagating from the lower atmosphere can reach amplitudes where they begin to break. Momentum is deposited and the resulting drag force has to be taken into account in addition to the forces considered in geostrophic equilibrium. This force equilibrium is sketched in figure 2.6.

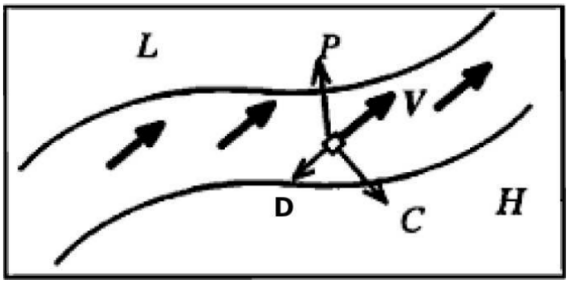

Figure 2.6: Quasi-Geostrophic equilibrium in the mesosphere, drag force D, pressure force P and Coriolis force C balance each other. Low pressure L, high pressure H, horizontal Wind V. Picture from Fuller-Rowell [1995]

Due to the wave filtering at lower altitudes the drag force is seasonally dependent. In the summer hemisphere the resulting wind is turned towards the equator and in the winter towards the pole. Hence the mesospheric motion forced by this wave-breaking, called the residual circulation, is from pole to pole. The motion out of the pole leads to adiabatic cooling in summer. In winter the convergence into the pole causes adiabatic heating. The dynamical mechanical forcing is strong enough to reverse radiative equilibrium and results in the mesospheric wind and temperature distributions seen in figure 2.5.

The role of of the planetary wave westward momentum, which supplements this gravity wave momentum, on the residual circulation in winter will be examined in this thesis.

Chapter 3

Data and Methods

3.1 MERRA

The data that were used in the following analysis are from NASA's Modern Era Retrospective Analysis for Research and Applications (MERRA) reanalysis data. Reanalysis means that spacially and temporally irregular data were assimilated to a regular grid using models. The selected set has a horizontal resolution of $0.5\,^\circ \times 0.7\,^\circ$ (latitude $\times$ longitude). The vertical grid component has 72 pressure levels from ground to 0.015 hPa (~ 80 km). Up to about 50 km (~ 1 hPa) MERRA is measurement driven. Above that it is purely model determined. (See Rienecker et al. [2011].) The data used in MERRA stretches from 1979 to present. The measurements include conventional observations, i.e. pressure, temperature, height and wind components from weather stations, balloons, aircraft, ships buoys and satellites. Radiance values were taken from satellite data. MERRA uses the Goddard Earth Observing System version 5.2.0 model and data assimilation system which is a finite-volume atmospheric general circulation model. The analysis is constantly updated in the sense that the forecast model is updated according to the current analysis values. Thereby a 6h update cycle is obtained. Wind and temperature data from 2008 and 2009 was used in this thesis. Daily averages were used such that tidal waves and other short period oscillations are removed. However, planetary wave oscillations with periods greater than one day are present in the data. Thus, this data forms the basis for the extraction of planetary wave amplitudes with height at 72° S. This latitude allows the direct comparison to measurements taken at Troll station.

3.2 Wavelets

To separate the periods of the planetary waves, wavelet transforms were used. Wavelet transforms are appropriate for measurements that contain nonstationary power at a wide range of frequencies. Similar to a Fourier transform wavelet transforms use a basis of complete (orthonormal) functions to decompose the data. In

both cases the inner product (i.e. convolution) of the respective functions and the data is calculated. The resulting projection is the contribution of the respective functions [Torrence and Compo, 1998]. In the case of Fourier transforms those functions are plane waves.

The "mother" wavelet ψ is a function that has zero mean and is localized in time and frequency space. All possible scalings $\psi_s(\xi)$ of the mother wavelet form the basis. For any real s (scale) this is defined as $\psi_s(\xi) \equiv |s|^{-b}\psi\left(\frac{\xi}{s}\right)$. ξ is the time variable and b gives the vertical scaling (usually $b > 0$ is used). Therefore no scaling bias is introduced that would downgrade the analysis, considering the uncertainty principle of signal processing (time resolution times frequency resolution greater than or equal to $1/2$). This is an advantage of wavelet analysis over for example a sliding box window used in Fourier analysis. To obtain time localization of the wavelet analysis, $\psi_s(\xi)$ is translated by t_t. Thus the result of the transform depends on translation time t_t and scale s. The scale can be transformed to frequencies by multiplying with a constant factor depending on the specific wavelet [Kaiser, 1994]. In the following discussion, a Morlet wavelet was used as shown in figure 3.1. A Morlet wavelet is a vertically shifted sine wave localized by a Gaussian window.

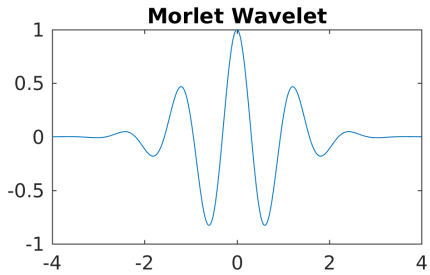

Figure 3.1: General example for a Morlet wavelet

Chapter 4

Problem and Results

4.1 Mid-Winter Cooling

Although the main physical mechanisms involved in the global circulation are understood, general circulation models are still challenged to fully explain all processes. As documented within several investigations (Gardner et al. [2011], Picone et al. [2002]) the down welling in the southern hemispheric polar region slows down and the warming in the mesosphere stops towards mid-winter. The mid-winter cooling can for example be seen in OH nighglow measurements at Rothera (68° S, 68° W) during 2002-2005, which represent the neutral temperature integrated over the ~ 8 km thick airglow layer near 87 km. They are shown together with WACCM model temperatures integrated over the modeled OH density for 2002-2005 in figure 4.1. Both datasets show an increase in temperature until May. Afterwards they fall off until July. The spring temperature decrease is visible in September.

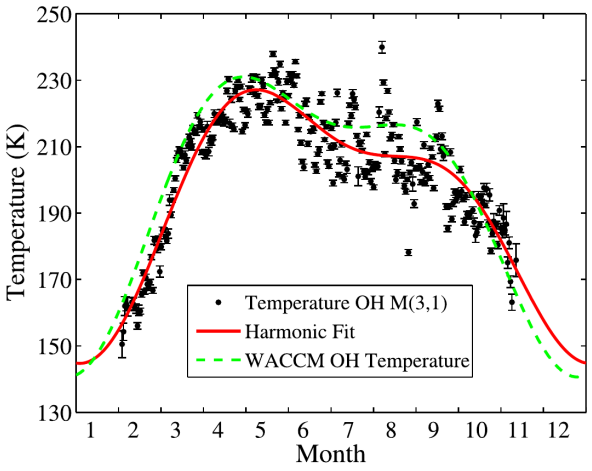

Figure 4.1: Time series of OH Meinel (3,1) band nightglow temperatures and their standard errors measured at Rothera during 2002-2005, the harmonic fit, and the WACCM modeled temperatures at 87 km. Taken from Gardner et al. [2011]

Temperatures at 87 km for 2008 and 2009 derived from MSIS data also show the mid-winter cooling as can be seen in figure 4.2. MSIS is an empirical, global model based on observations and driven by seasonal and solar and auroral conditions [Picone et al., 2002]. Both figures show an increase in temperature from mid-summer (January) towards early-winter (May) and a cooling from late-winter (August) to summer (December) as expected from the basic global circulation theory (see Section 2.3). However during mid-winter (June-July) where the theory expects the highest temperatures a cooling is visible instead.

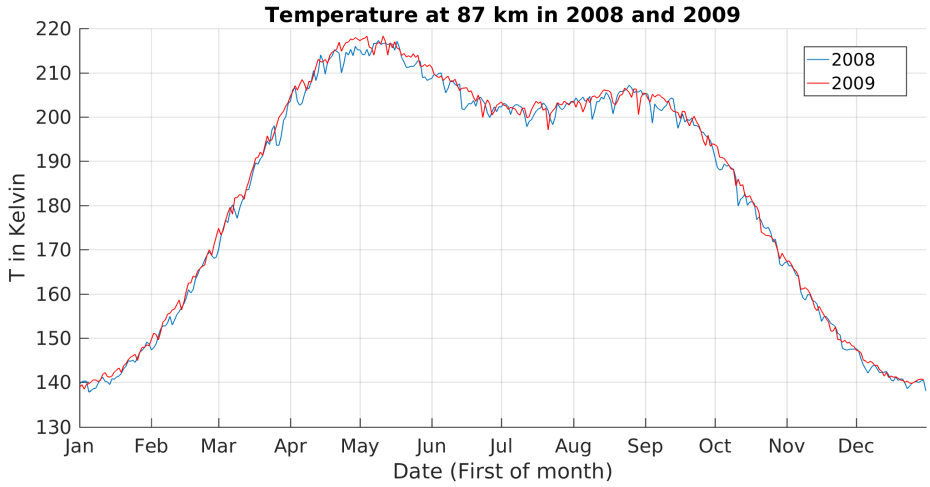

Figure 4.2: Daily averaged temperatures above Troll station at 72.01 °S, 2.5 ° W at 87 km altitude in 2008 (blue) and in 2009 (red) derived from MSIS data [Picone et al., 2002].

Finally, the temperatures derived from meteor trail diffusion are shown in figure 4.3 for radars at Rothera (68° S, 68° W) and Trondheim (64° N, 10° E) (from Espy [2016]). The diffusion coefficient of meteor trails is temperature dependent such that the temperature can be derived from decay times [Hocking, 1999]. Both stations show similar temperature behavior in autumn and spring. The southern hemisphere temperatures from Rothera show a distinct mid-winter cooling dip whereas their northern hemisphere counterparts show highly variable winds during mid-winter. This northern hemisphere variability is due to the weaker polar vortex and stronger planetary wave activity as the orographic forcing is stronger. The two aspects together cause Sudden Stratospheric Warming events typical of the northern hemisphere, where the polar vortex is broken down by strong planetary wave activity.

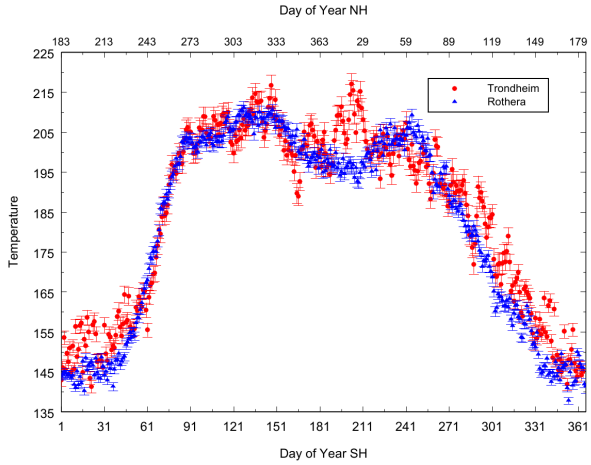

Figure 4.3: Temperatures derived from meteor trail diffusion above Rothera (68° S, 68° W) and Trondheim (64° N, 10° E). [Espy, 2016]

4.2 Slowing residual circulation

The observation of the cooling coincides with a slowing of the meridional wind and the corresponding downward motion at the winter pole [Espy et al., 2003]. The meridional wind derived from the Horizontal Wind Model (HWM-93) , which is an empirical data model with the same drivers as the MSIS model [Hedin et al., 1996] is shown in figure 4.4. For the wind at 75 km the wind stagnates at about the same value between April and August. The wind at 80 km even shows a slight weakening in that time frame.

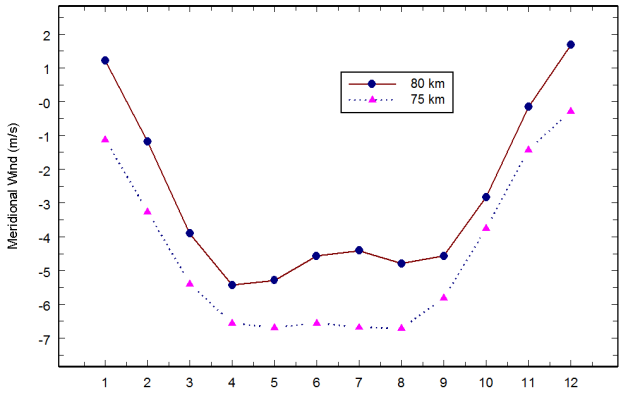

Figure 4.4: Meridional wind above Rothera based on the Horizontal Wind Model (HWM-93). [Hedin et al., 1996]

To illustrate the slowing vertical motion, volume mixing ratios of carbon monoxide (CO) obtained from BAS (British Antarctic Survey) radiometer measurements at Troll station (72.01 °S, 2.5 °W) in 2008 and 2009 are given in figure 4.5 [Straub et al., 2013]. CO has a steady increase in volume mixing ratio (vmr) with altitude

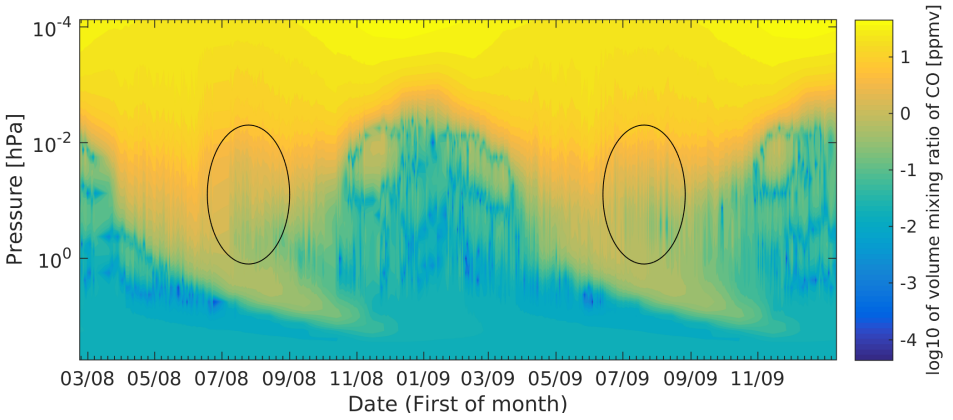

Figure 4.5: Smoothed volume mixing ratio of CO above Troll station. Data from Straub et al. [2013]

and from pole to pole. The steady gradient is a result of CO being the product of photodissociation of CO_2 at high altitudes, but having a high dissociation energy itself. Due to reduced photodissociation at polar latitudes a steady vertical gradient can be assumed between $30 - 80$ km altitude. During winter when the polar vortex is present, changes in CO vmr can be assumed to be related to vertical motion, even though the mixing ratios develop differently within the polar vortex and mid-latitudes because of the different illumination conditions [de Zafra and Muscari, 2004]. This is due to the strong barrier against latitudinal mixing that occurs at the vortex edge. Within the vortex the volume mixing ratio is higher than at mid-latitudes and its vertical gradient is controlled by the descending motion within the vortex. Later in spring, the polar vortex at high altitudes weakens and horizontal mixing can occur. In this case the influence of vertical and horizontal motion on the mixing ratio cannot be distinguished clearly. When the vortex is fully broken down the horizontal CO vmr gradient is relatively small [Hoffmann, 2012].

Figure 4.5 is derived from data at 72°S. For both years it can be seen that from March until July the mixing ratio increases at the same pressure level, indicating downwards motion. Then a decreasing trend can be recognized for a short time (See circles). This decrease indicates slowing downward motion or even upwards motion. Afterwards the vmr stays at about the same level respectively slightly higher. As this rather stagnated behavior occurs in September, it might be caused by horizontal motion transporting CO poor air into higher latitudes as then polar vortex weakens. Therefore it may not be solely vertical motion. In 2008 the increase in CO from March on is higher and falls off more steeply in June than in 2009.

4.3 Link to planetary waves

Since the vertical and meridional wind change, momentum deposition by planetary waves may be the cause. Plumb [1989] investigated the seasonal behavior of planetary waves of zonal wavenumber 1 for settings corresponding to the two hemispheres in a model. He assumed stationary waves and uses a trunctuated β-plane approximation. That means approximating the latitudinal variation of the Coriolis parameter linearly and thereby using Cartesian coordinates. As shown in figure 1.2(a), a relative minimum of wave amplitude in mid winter is obtained for weak forcing by waves. A single continuous maximum is found for strong wave forcing (figure 1.2(b)).

The observation of the vertical wind in figure 4.5 is in accordance with the interpretation in Plumb [1989]. For weak wave forcing characteristic of the southern hemisphere Plumb finds, that the mean zonal wind is nearly unperturbed. Under these conditions, the background flow becomes stronger than the Charney-Drazin criterion such that waves cannot propagate into the mesosphere. This reduces the westward momentum wave drag in the mesosphere and results in a reduction of the flow in meridional direction and consequently cooling of mesospheric temperatures. On the other hand, if the forcing is strong, as it typically is in the northern hemisphere, the mean flow is weakened and waves can propagate upwards. This would account for the differences in the mesospheric temperatures in the two hemispheres observed in figure 4.3, and indicates that changes in the southern hemisphere planetary waves at high altitudes may be the cause of the observed mid-winter cooling.

The Charney-Drazin criterion gives lower critical velocities U_c for faster waves (2.2). From this and Plumb's argumentation it is expected to see how fast waves are blocked before slower ones in southern hemisphere winter.

4.4 Wave extraction

To investigate whether the planetary waves actually are blocked we want to know how strong planetary waves are at different altitudes throughout winter and which periods are found. To do so, first zonal fits to the zonal wind u of the form

$$\bar{u} + a_1 \cos\left(\frac{2\pi \cdot long}{360^\circ} + \varphi_1\right) + a_2 \cos\left(\frac{2\pi \cdot long}{180^\circ} + \varphi_2\right) + a_3 \cos\left(\frac{2\pi \cdot long}{120^\circ} + \varphi_3\right) \tag{4.1}$$

were performed using MERRA zonal wind data (Rienecker et al. [2011]) at 72° S at each pressure level for every day in 2008 and 2009. This fit accounts for planetary waves with zonal wavenumber 1,2 and 3 (termed the s1, s2 and s3 components) and a mean background flow.

The results for the amplitudes at 55 km, 40 km and 25 km are shown in figure 4.6. Overall the fit shows high day to day variability. It can be seen, that the wave activity for all components increases until June. Then it falls off by up to 60 % compared to before the fall off. In September/late August the waves become stronger again and peak up to $1.5 - 2$ times as strong as before the fall-off, which

is particular visible at 40 km for the s1 and s2 component. From 25 km to 40 km an increase in waveamplitude can be seen. At 55 km compared to 40 km the amplitudes become lower again and the winter dip is less clear. That can be due to reduced wave activity. Otherwise it might be due to the used data. As MERRA is model driven at this altitude day to day features such as waves may be less accurately resolved. The s1 component carries most wave amplitude. A closer look at the amplitudes will be given in chapter 5.

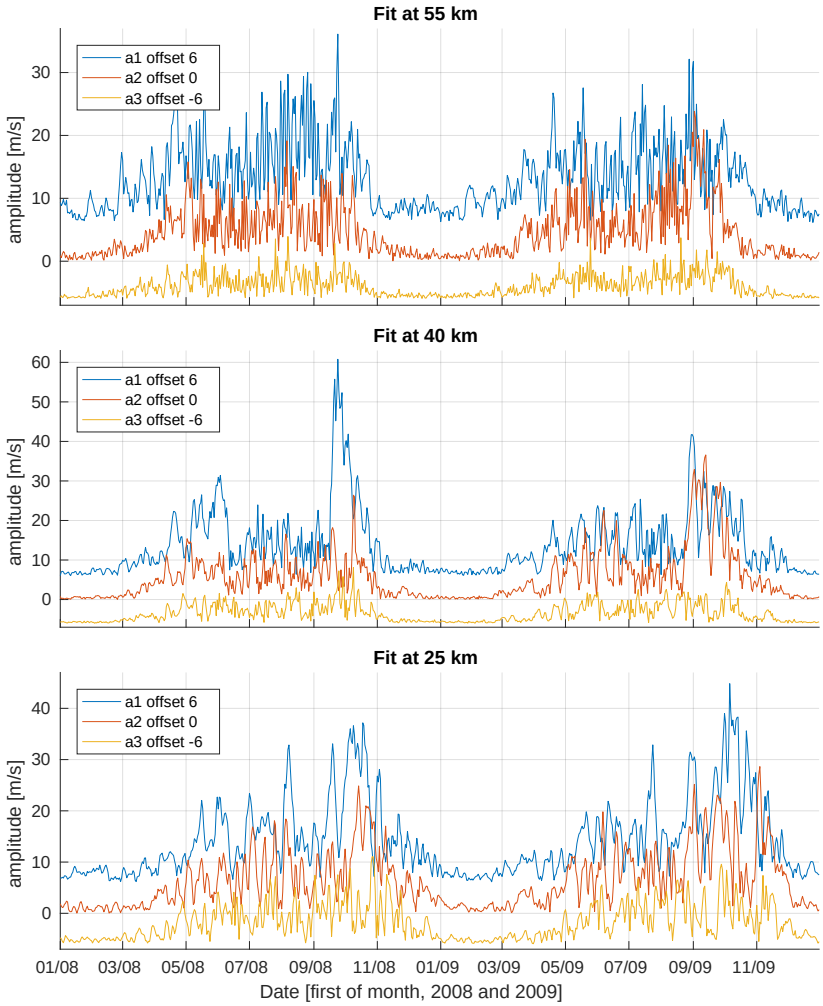

Figure 4.6: Amplitudes of the fitted sines to the daily zonal wind in 2008 and 2009 at 72° S . The top plot is at 55 km, the middle at 40 km and the bottom at 25 km altitude. Given are the amplitudes of the fitted s1, s2 and s3 component (with offsets for better visibility).

The next question is, how the s1, s2 and s3 components progress zonally in 2008 and 2009 during winter. Figure 4.7 shows the time-longitude plots for the s1, s2 and s3 waves from autumn through spring. 40 km was chosen as altitude as it can be seen from figure 4.6 that wave activity is quite strong at this altitude. Slight differences in the two years are visible. In 2008 the s1 component shows stronger wave activity and zonal progression before midwinter whereas in 2009 this happens after midwinter. During June and July for the s1 and s2 components episodes of little zonal propagation can be seen. The s3 component shows little trend. But the s3 component is often dominated by the quasi 2-day wave and it cannot be expected to resolve the propagation well in daily data as used here [Limpasuvan et al., 2000].

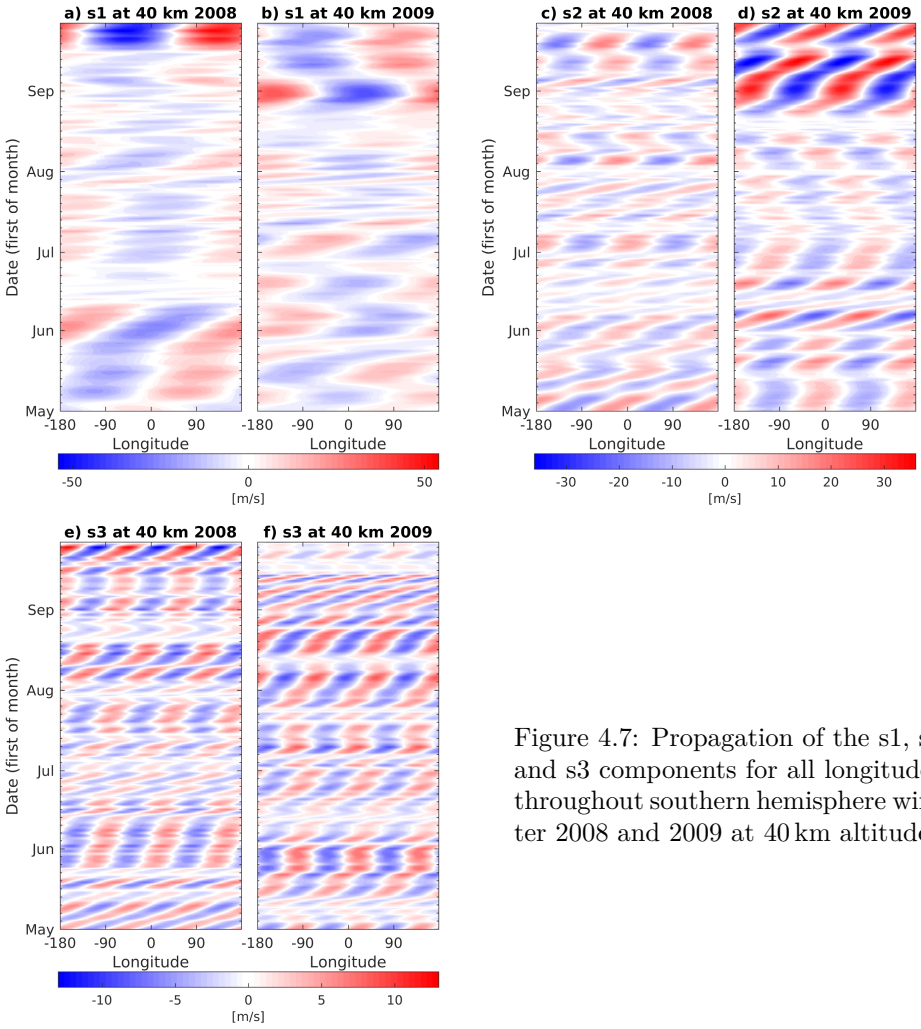

Figure 4.7: Propagation of the s1, s2 and s3 components for all longitudes throughout southern hemisphere winter 2008 and 2009 at 40 km altitude.

A quantitative approach to the propagation follows in the next step. Each zonal wavenumber component consists of several temporal components with different horizontal phase velocities. Therefore each of these components could cut off at different wind speeds. To separate the different wave periods and examine how they vary throughout the year, a wavelet transform of the s1 and s2 components of both years was employed. Wavelets as a method were explained in section 3.2. Since the strongest s3 component is the quasi 2-day wave, it was not possible to isolate this wave component using daily averaged data since it is at the Nyquist frequency. Therefore only the s1 and s2 component were considered here. The selected longitude was 2° W (above Troll station). The significance levels of the results relative to red noise were set to 0.95 in the analysis. The result of the analysis for the s1 wave in 2008 at 25 km altitude and 51 km is found in figure 4.8. At 25 km altitude the wave power is predominantly at long periods. At 51 km shorter periods are stronger and the longer ones became weaker. A similar behavior is found for the s2 component (Figure 7.1 in Appendix).

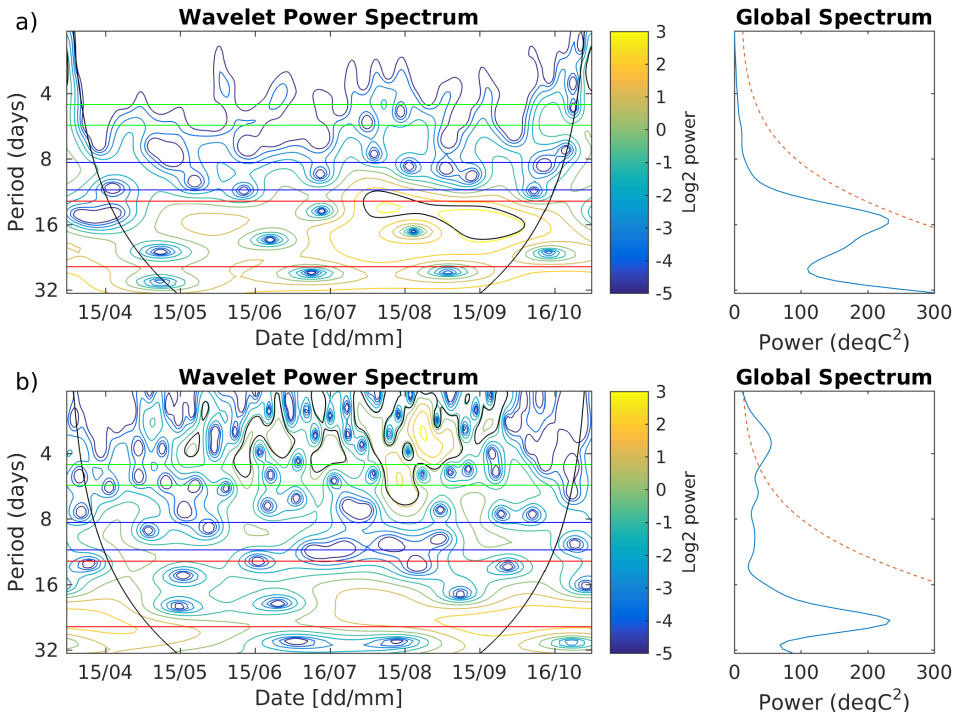

Figure 4.8: Wavelet analysis of the s1 wave for 2008 at a) 25 km altitude and b) 51 km. Each with the wavelet power spectrum on the left. The results outside the black cone are subject to boundary effects. The black contour lines mark the significance level. On the right is the global spectrum with the significance level as dashed line. The horizontal lines mark the integration ranges for Doppler shifted 5-, 10- and 16-day waves. See also table 4.1.

Planetary waves can be subject to Doppler shifting, such that a band in the wavelet power spectrum belongs to one wave period. To account for this, a weighted average of the wave power over the range of possible frequencies was performed following Torrence and Compo [1998]. The frequency ranges are given in table 4.1 based on Salby [1981].

Wavenumber	Wave period	Lower limit [1/days]	Upper Limit [1/days]
s1	5 day	4.5	5.6
s1	10 day	8.3	11.1
s1	16 day	12.5	25
s2	4 day	3.7	4.3

Table 4.1: Range of Doppler shifted frequencies for the investigated waves. Based on Salby [1981]

Still, the wave power in figure 4.8 does not clearly stay within those frequency limits. That can be seen in the overlap in wave power between the 10- and 16-day wave at 25 km. The short period wave power at 51 km also shows power at periods shorter than the expected 4 and 5-day waves. This might be due to short period 3-day and 4-day oscillations of zonal wavenumber 1 and 1.5 to 2 day oscillations of wavenumber 2 that have been observed in the polar winter stratosphere for example in Prata [1984].

The time-altitude plots with the integrated wave power across the bands from table 4.1 are given in figures 4.9 and 4.10. The 10-day wave and 16-day wave originate from low altitudes and seem to propagate up to certain limits for the selected altitude range in figure 4.9. Both waves show a weakening in midwinter around June and July in both years. In 2009 wave power is remains stronger at higher altitudes before and after mid-winter than in 2008. This is consistent in the sense that differences between the years could already be seen in the CO measurements (figure 4.5).

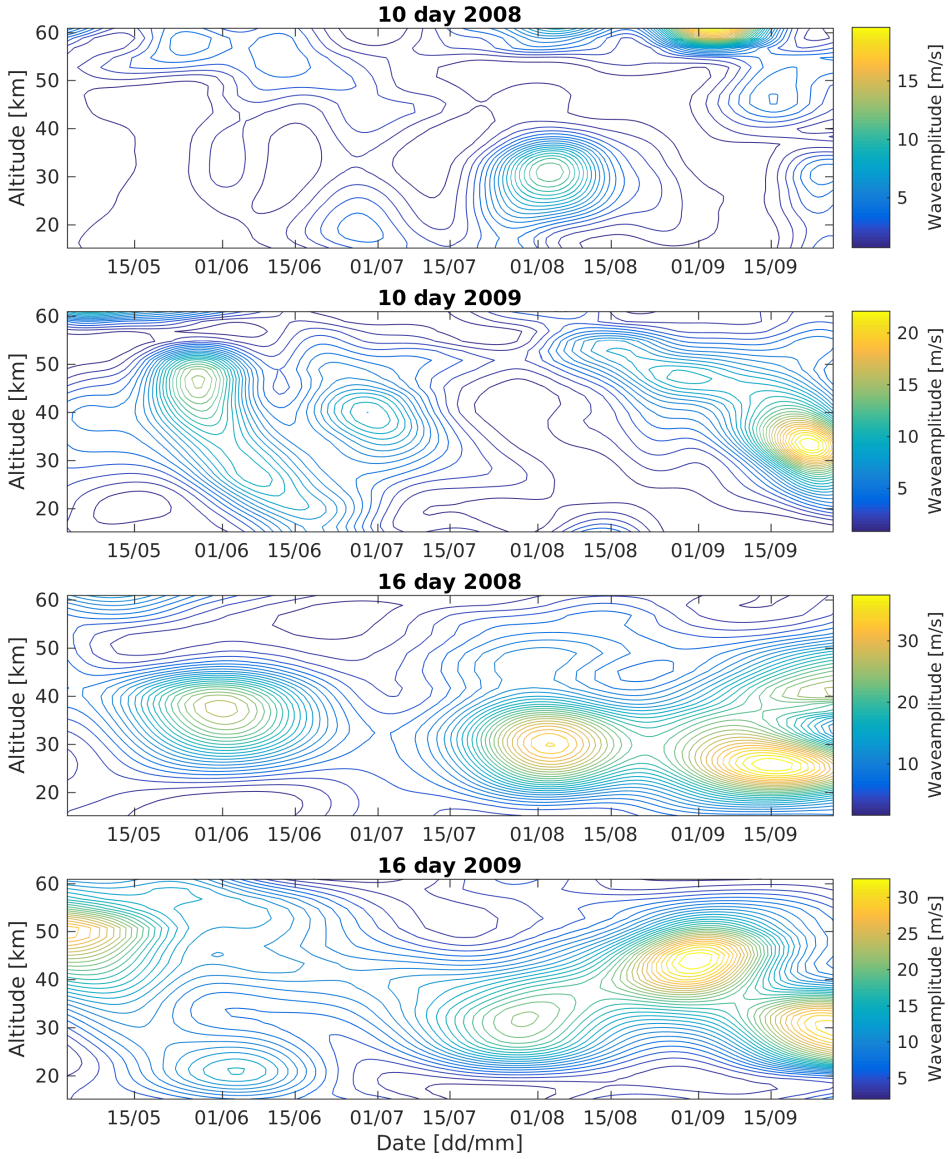

Figure 4.9: Weighted average of the wave power for the Doppler shift range for the 10-day and the 16-day wave in 2008 and 2009 at 72° S.

The time and altitude dependence of the short period 4- and 5-day waves are given in figure 4.10. The 5-day wave shows little power at low altitudes. However, it does show bursts of large amplitudes near mid-winter above 45 km. Therefore the waves are likely generated at altitudes above 40 km due to steep wind gradients and do not originate from low altitudes.

Also shown in figure 4.10 is the 4-day wave. It has most power above 50 km. Bursts of activity are found throughout the year. Hence it can be assumed that it is also generated at high altitudes. In mid-winter the wave power tends to start being present already at lower altitudes.

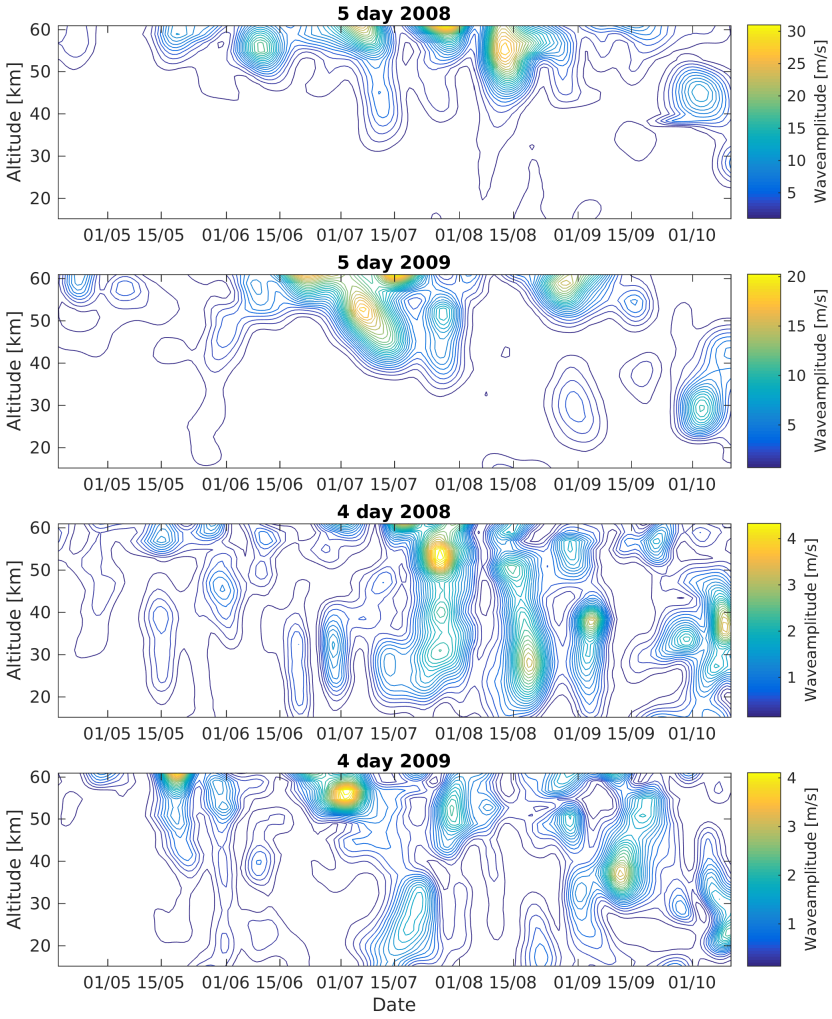

Figure 4.10: Weighted average of the wave power for the Doppler shift range for the s1 5-day and the s2 4-day wave in 2008 and 2009 at 72° S.

4.5 Mean wind

To obtain further insight into the observations in figure 4.9, the phase velocities c and critical velocities U_c are calculated in table 4.2 using formula 2.1.

Wave period	c [m/s]	U_c [m/s]
5 day	28.7	13.4
10 day	14.3	27.7
16 day	9.0	33.1
4 day	17.9	

Table 4.2: Phase velocities and critical velocities

These values for U_c are related to the zonal mean zonal wind which was obtained from the constant terms in the fit of the planetary waves to the data given in equation 4.1. The contour plots for both years are given in figure 4.11 with the values for the critical velocities highlighted. The critical velocities are located at higher altitudes in 2009. Recalling that it could be seen in figure 4.9 that the 10-day wave and the 16-day wave propagate higher in 2009 this is a rough indication that the waves actually are reflected by the mean flow. In both years the zonal mean zonal wind has a similar pattern as the mean wind in the weak wave forcing case in Plumb [1989], that is rather smooth and without strong perturbations (figure 1.2(c)).

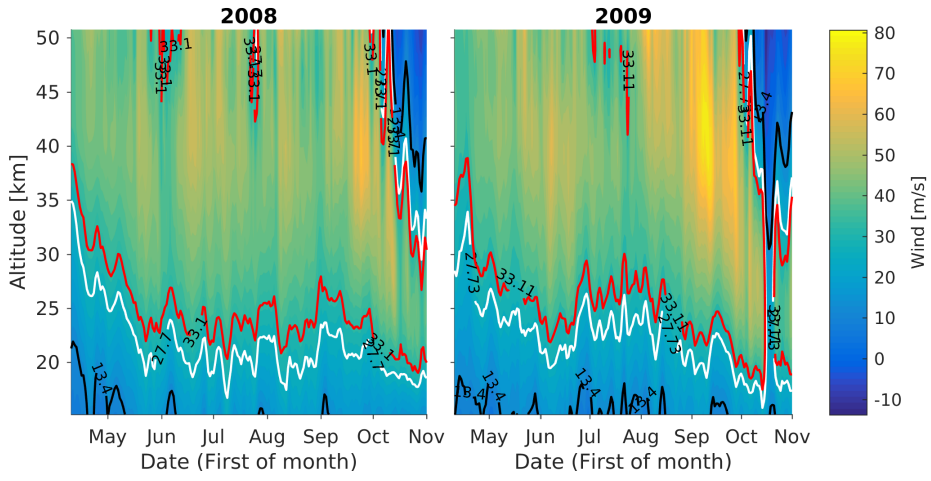

Figure 4.11: Zonal mean zonal wind for mid year 2008 and 2009 from fit. The highlighted lines are the critical velocities of the 5-day wave 13.4 m/s (black), 10-day wave 27.7 m/s (white) and 16-day wave 33.1 m/s (red). Based on formula 2.1.

However, it could be seen from figure 4.6 that planetary waves are found above the altitudes marked in figure 4.11. The values for U_c are below the actual physical

values as it is often the case since it is a very simple model [Brasseur and Solomon, 2005] and the β-plane approximation is becoming less valid at higher latitudes. Therefore formula 2.2 was also used to determine which regions the planetary waves can enter. The critical velocity for stationary waves relative to the mean wind is given in figure 4.12. Stationary waves can be seen as the boundary case for slow waves. Therefore it can be said, that regions that block stationary waves, cannot be entered by any planetary waves.

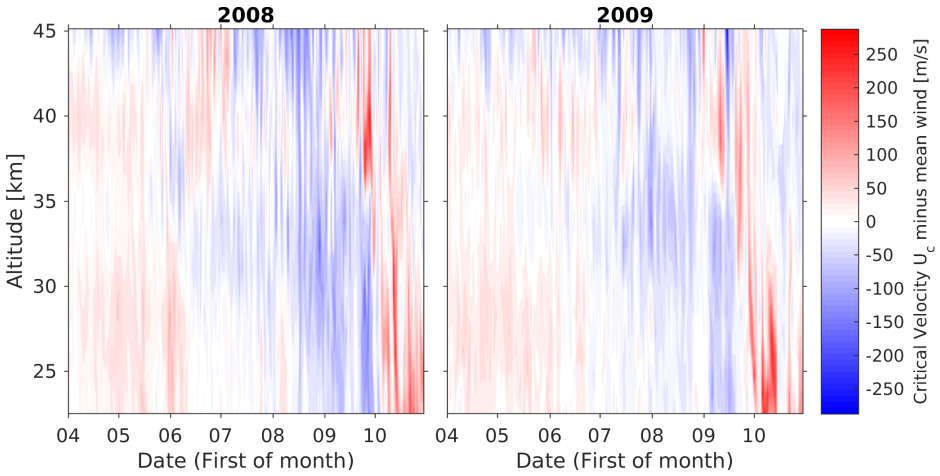

Figure 4.12: Critical velocity relative to the mean wind calculated from formula 2.2 for stationary waves. Red regions allow wave propagation, blue regions do not.

In both years, wave propagation is expected from low altitudes to above 40 km until mid-June. During mid-winter a blocking layer is present at 30 km preventing propagation from below. Around September conditions allowing wave propagation are found at ca. 40 km and move downwards towards October. Until September those model calculations agree with the wave amplitudes in figure 4.6. As the spacial spacing of MERRA is bigger at higher altitudes, the numerical differentiation decreases in accuracy.

Both calculations of the critical velocities have their limitations as they are based on model assumptions. As only a slice at one latitude was considered the focus is solely on vertical propagation. Both calculations indicate that vertical wave propagation from low altitudes is expected to decrease from May to June.

Chapter 5

Discussion

5.1 Overview

So far it has been documented, that the southern hemisphere mesosphere cools in mid-winter and the poleward flow is weakened. This means that less westward momentum reaches the mesosphere. The initial question was whether the cause is that planetary waves are blocked by strong stratospheric winds as these winds can reach speeds exceeding the upper limit of the Charney-Drazin criterion.

Therefore fits of the s1, s2 and s3 component were applied to MERRA zonal wind data. The weakening in the wave amplitude in mid-winter could be seen (figure 4.6), which supports the hypothesis that the polar vortex winds reflect the planetary waves. Also a strong burst of wave activity after the weakening was found, in particular at 40 km. The decomposition of the 4, 5, 10 and 16-day wave components, presented in figures 4.9 and 4.10, has shown that the short period 4- and 5-day components seem to be generated in-situ at altitudes near 50 km as they are only found above 40 km with negligible amplitudes below this.

Waves can be generated by baroclinic instabilities caused by shears due to steep gradients of the zonal wind. Such gradients are present above the wind maximum at 40 km in mid-winter [Hibbins et al., 2005] and could give rise to the 4- and 5-day waves found above. The climatology for the zonal wind above Rothera station is given in figure 5.1.

To examine those gradients in detail, figure 5.2 shows the vertical and horizontal zonal wind gradients for 2005 for around 70°S [Baumgaertner et al., 2008]. It can be seen in the figure that the wind shears build towards mid-winter, with vertical shears concentrated at or on the top-side of the wind maximum near 40 km. Although the horizontal shears occur both above and below the wind maximum shown in figure 5.1, waves generated below would be blocked by the strong winds at the maximum. As the climatology wind in figure 5.1 and the 2005 wind gradients in figure 5.2 agree, those assumptions are also valid for 2008 and 2009.

Thus, the strong short period wave burst seen at mid-winter at high altitudes is likely due to in-situ generation by the baroclinic instabilities above the stratospheric

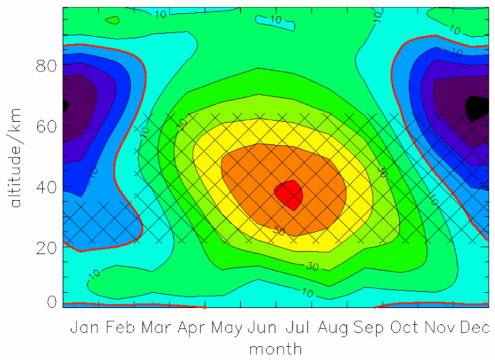

Figure 5.1: Climatology mean zonal wind above Rothera from 0–100 km. Generated from 6th order polynomial fits to the monthly mean data and, within the hatched area, monthly mean HWM-93 model winds. The thick red line represents the 0 ms^{-1} contour, other contours are drawn at 10 ms^{-1} intervals (blue: westwards). From Hibbins et al. [2005]

wind maximum.

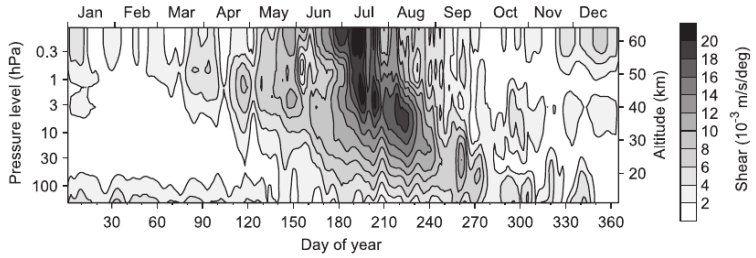

(a) Average vertical wind shear between 60° S and 70°S during 2005, derived from MLS temperature measurements.

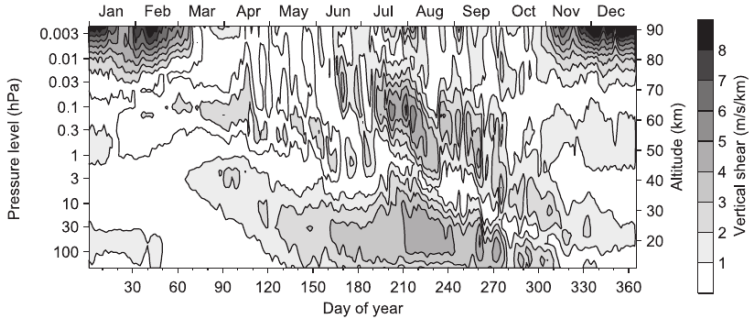

(b) Horizontal wind shear at 70° S during 2005, derived from UKMO zonal wind data.

Figure 5.2: Southern hemisphere wind shears from Baumgaertner et al. [2008].

On the other hand, the long period waves seen in figure 4.9 are present at lower altitudes (below about 45 km in 2008 and 50 km in 2009). They have their highest altitude extend and most power in the beginning and end of winter. The slower 16-day wave tends to reach higher than the faster 10-day wave. That is

indicative of the waves reaching the upper end of the Charney-Drazin criterion as the faster waves would be blocked by slower eastward winds. The mean wind roughly supports that as the calculated cut-off winds are found at lower altitudes for 2008 than for 2009 as can be seen in figure 4.11).

The calculations for the critical velocities given in figure 4.12 suggest that waves can propagate upwards until June. Fom then until October a blocking layer is found at 30 km.

5.2 Interpretation of the results

Altitude profiles of polar southern hemispheric temperatures above Rothera, presented in figure 5.3, show that the cooling in mid-winter appears up from about 60 km. The 4- and 5-day waves form close to this altitude and it is therefore unlikely that they have an impact on the cooling. They are still small in amplitude at this altitudes and would have a small impact if for some reason they would break at these altitudes. Therefore their momentum deposition is unlikely to be the driver for the meridional circulation. Hence it is reasonable to look at altitudes below 40 km when discussing the overall amplitudes of the s1, s2 and s3 components.

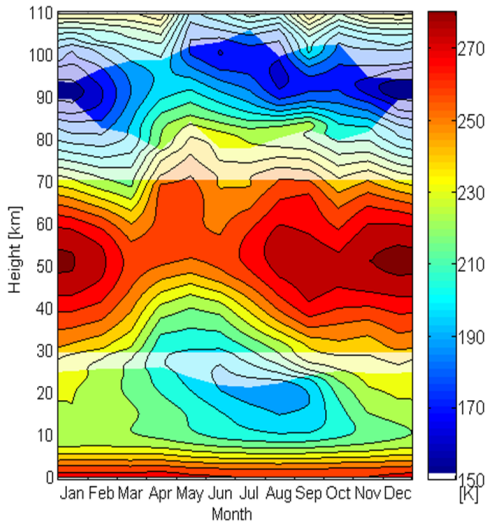

Figure 5.3: Temperature measurements above Rothera. The gray areas on the graph are interpolation, while the brighter areas are measurements. The highest altitudes are from the Fe resonance lidar, middle altitudes are temperatures from the Rayleigh lidar, and the lowest altitudes are temperatures from radiosonde balloons. From [Dietrich].

To test whether the polar vortex winds actually block the planetary waves, we look at the wave amplitude relative to the CO measurements and relative to the mean wind. The s1 component is the main indicator, as it carries most planetary wave amplitude and momentum. The s2 wave component is taken into account as it showed similar behavior to the s1 component in terms of short periods dominating

at high altitudes and longer ones at lower altitudes (figure 7.1). Considering both gives a clearer result. So far the 4-day wave was considered for the s2 component. But lower frequencies can also be found that could be observed using our daily sampling. (Salby [1981], Madden [1979]). However, as the s3 component was already left out in the wavelet analysis, it is again left out as it consists mostly of the quasi 2-day wave which cannot be resolved in our daily data, and which is known to be generated by baroclinic instabilities [Limpasuvan et al., 2000]. The wave amplitude was taken at a single altitude instead of integrating several to avoid mixing in other effects as for example reflected waves. 40 km were selected as altitude since the long period waves were very clear at that altitude, but the short period waves are left out.

In figure 5.4 (a) the CO vmr measurements that were shown in figure 4.5 are sampled at the at 70 km altitude and shown together with the summed amplitude of the s1 and s2 wave amplitudes at 40 km for 2008. 70 km is used since the mid-winter cooling is present at that altitude (figure 5.3) and any change in vertical motion and therefore CO vmr should be visible.

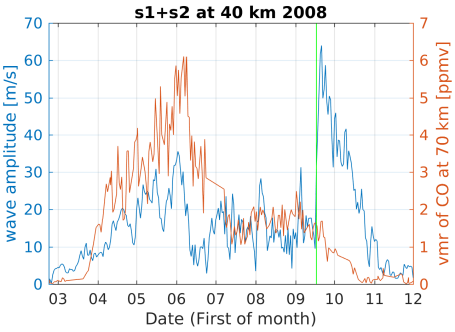

(a) Wave amplitude s1+s2 at 40 km (blue) and volume mixing ratio of CO at 70 km (red) in 2008.

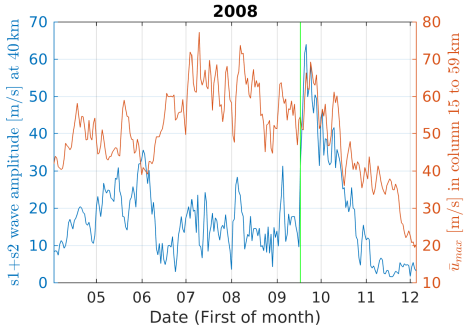

(b) Wave amplitude s1+s2 at 40 km (blue) and maximum zonal mean zonal wind in column from 15 km to 60 km (red) in 2008.

Figure 5.4: CO measurements, mean wind and wave amplitude 2008. The green line marks 17-Sep-2008.

Until mid-September the CO vmr and the wave amplitude follow each other. That supports the hypothesis that increasing (decreasing) westward momentum deposited by planetary waves creates stronger (weaker) descent indicated by the changes in CO. However, after the middle of September the wave amplitude peaks and the CO vmr falls further. Since the CO measurements are not in daily intervals, they have to be interpolated to calculate the correlation coefficient. For the interval from 23-Feb-2008 to 17-Sep-2008 the correlation coefficient is found to be 0.66 with a p-value of 5×10^{-21}. This quantifies the degree to which changes in planetary wave amplitudes are accompanied by changes in the vertical motion. However, it should be noted that the correlation coefficient tests only the degree to which changes in the quantities are linearly dependent, even though there may be a higher order dependencies between the variables.

In figure 5.4 (b) the maximum zonal mean zonal wind in the column from 15 km to 60 km and again the sum of the s1 and s2 wave amplitudes are plotted. Again until mid-September, it can be recognized that the behavior of the wave amplitude is opposite to that of the maximum wind, which is particular visible from mid-May throughout June. This anticorrelation supports the case that the strong eastward winds block wave propagation. However, similar to figure 5.4 (a) a change occurs from mid-September. The maximum mean wind and the wave amplitude start to be correlated rather than anticorrelated.

The same analysis has been performed for 2009 and is shown in figure 5.5. The dip in the wave amplitude in figure 5.5 (a) in mid-winter is less pronounced in 2009 than in 2008. Still the rise in wave amplitude and in CO vmr coincide before winter and both fall off in June and August. Again, during September the correlation breaks and the wave amplitude rises while the CO volume mixing ratio falls off. In 2009 that happens at the beginning of September rather than mid-September in 2008. The correlation coefficient of the wave amplitude and the CO volume mixing ratio for the interval from 23-Feb-2009 to 27-Aug-2009 is correspondingly slightly less, 0.61 with a p-value of 3×10^{-27}.

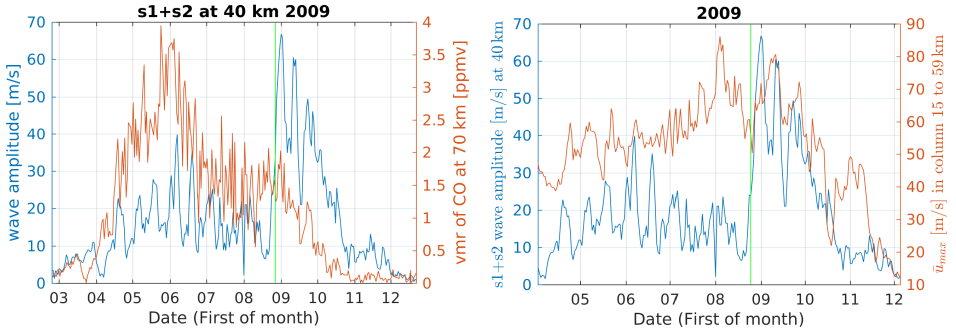

(a) (b)

Figure 5.5: Same as figure 5.4 for 2009. The green line marks 27-Aug-2009

The anticorrelation between maximum mean wind and wave amplitude can also be seen in 2009, but not as clearly in the day-to-day features as was observed in 2008. However, generally speaking, the mean wind becomes stronger from mid June to beginning of August while the wave amplitude decreases. Overall both 2008 and 2009 support the hypothesis that planetary waves are blocked from the mesosphere by the stratospheric zonal wind maximum and less westward momentum is supplied to the residual circulation. The effect is more evident in 2008 in all indicators than in 2009, where it is more varied. From September onward there appears to be another process at work, and the hypothesis of a direct link between planetary wave amplitude and the residual circulation is not supported.

Different effects might contribute to the correlation break off from September on. In figure 4.12 calculations suggested that conditions favoring wave propagation appear at 40 km in September while lower in the atmosphere unfavorable conditions

persist. Therefore horizontal wave propagation at high altitudes might be relevant to the recovery of the residual circulation in spring.

Another effect to consider is that horizontal mixing of CO might start to occur. As explained in Hoffmann [2012], the polar vortex acts as a barrier for horizontal mixing of CO. The polar vortex usually begins to break down in late October or early November [Hibbins et al., 2005]. As the polar night ends the shadow height lowers in the atmosphere. Due to the heating the temperature gradient becomes weaker and therefore the zonal wind weakens starting from high altitudes. Hence the polar vortex already starts to weaken in September at high altitudes and thus horizontal mixing of CO becomes possible.

In addition, the short wavelength waves from high altitudes might weaken the vortex. Since they appear strongly in mid-winter they might influence the temperature recovery in late winter. Again, a weaker vortex allows for horizontal mixing.

Furthermore, the maximum wind becomes weaker and is found at lower altitudes in late winter as seen from figure 5.1. Therefore the maximum might shift below the region of long wavelength planetary wave generation and does no longer affect the waves.

Chapter 6

Conclusion

The initial question was what causes the mid-winter cooling in the mesosphere in the southern polar region. As the westward momentum deposited by waves in the polar mesosphere forces a residual poleward motion and subsequent adiabatic heating in winter, measures to discuss the cooling are the poleward motion and planetary wave activity. The planetary wave activity provides additional westward momentum that drives the residual circulation further away from radiative equilibrium.

A decrease in planetary wave amplitude for zonal wave numbers 1, 2 and 3 in mid-winter (June-August) could be shown using MERRA zonal wind data for 2008 and 2009. The decrease in planetary wave activity coincided with the change in the vertical motion traced with CO and the cooling visible in the southern hemisphere temperatures. The hypothesis that the reduction of westward momentum from planetary waves was a cause for the slowing residual circulation was supported by the correlation of the s1+s2 wave amplitude and CO vmr until the beginning/middle of September.

We tested if the planetary wave activity decreased because the stratospheric wind reached the upper limit of the Charney-Drazin criterion and blocked vertical propagation of planetary waves, as suggested by Plumb [1989]. As one indicator the mean stratospheric wind was found to be strongest when the planetary wave activity is weakest. In addition, the Charney-Drazin criterion was calculated using the MERRA mean wind as a function of time and altitude, taking the wind shear into account. The decrease in mid-winter in planetary wave amplitude coincided with with periods when the calculated Charney-Drazin limit indicated that that the waves should be cut off below the stratopause. Furthermore, the wavelet analysis showed that the different period waves, with their different phase velocities, were cut off consistent with the calculated Charney-Drazin criterion since faster waves were cut off at lower altitudes.

Therefore I conclude, that until late winter the stratospheric winds reach speeds high enough to reflect the planetary waves at low altitudes according to the Charney-Drazin criterion and prevent them from reaching mesospheric altitudes. As less westward momentum is provided to the mesosphere, the residual circulation slows

and the adiabatic heating reduces.

However, from September/late August onward the correlation of the planetary wave amplitude with the CO, the maximum wind and the Charney-Drazin criterion breaks down. It is likely that the lack of correlation with the CO is explained by horizontal mixing of CO that has been observed to occur during this time such that it no longer acts as a tracer for vertical motion [Hoffmann, 2012]. To explain the de-coupling of planetary waves from the mean winds, we note that the Charney-Drazin calculations show regions of favorable conditions for planetary waves at high altitudes in September before descending during spring. Thus those regions for favorable propagation would be expected to extend to lower altitudes at lower latitudes during this time. Therefore I suggest that planetary waves from lower latitudes could migrate horizontally into the polar regions (Forbes et al. [1995], Dickinson [1968]) and would not be blocked vertically by the stratospheric winds investigated. Although left as a suggestion for future work, I suggest that this breakdown in the relation between planetary wave amplitude and the maximum stratospheric wind, CO vmr and the Charney-Drazin criterion is due to both horizontal mixing of CO and planetary wave propagation from lower latitudes.

Chapter 7

Further Research

It could be shown that the CO vmr, mean zonal wind and wave amplitude correlate until end of August/mid September pointing towards the mean wind blocking the planetary waves as the cause for the mid-winter cooling. However, afterwards the correlation breaks off and other effects start to dominate at this time. Some possible causes were considered in chapter 5.

Future investigations into what the specific drivers are, could look into atmospheric models such as WACCM to investigate whether the late winter break up of the correlation of CO, planetary wave activity and mean wind can also be observed there. This would also allow to use diagnostic quantities such as the Elissan-Palm flux. By doing so, a more detailed analysis of the heat and momentum transport by planetary waves can be performed.

Our focus was on vertical propagation of planetary waves. Therefore it remains an open question whether momentum deposition from other sources such as gravity waves and tidal waves is becoming important in the late-winter recovery. Also horizontal propagation of planetary waves from lower latitudes could play a role in the recovery.

Bibliography

Andrews, D. G. (2010). *An Introduction to Atmospheric Physics*. Cambridge University Press, Cambridge, U.K. 2nd Edition.

Andrews, D. G., Holton, J. R., and Leovy, C. B. (1987). *Middle Atmophere Dynamics*. Academic Press, Inc.

Baumgaertner, A. J. G., McDonald, A. J., Hibbins, R. E., Fritts, D. C., Murphy, D. J., and Vincent, R. A. (2008). Short-period planetary waves in the Antarctic middle atmosphere. 70(10):1336–1350.

Brasseur, G. P. and Solomon, S. (2005). *Aeronomy of the Middle Atmosphere*. Chemistry and Physics of the Stratosphere and Mesosphere Series. Springer.

Charney, J. G. and Drazin, P. G. (1961). Propagation of planetary-scale disturbance from lower into upper atmosphere. 66(1):83–109.

de Wit, R. J. (2015). *Quantifying the influence of the stratosphere on the mesosphere and lower thermosphere*. PhD thesis, Norwegian University of Science and Technology, Faculty of Natural Sciences and Technology, Department of Physics.

de Zafra, R. L. and Muscari, G. (2004). Co as an important high-altitude tracer of dynamics in the polar stratosphere and mesosphere. *Journal of Geophysical Research: Atmospheres*, 109(D6):n/a–n/a. D06105.

Dickinson, R. E. (1968). Planetary rossby waves propagating vertically through weak westerly wind wave guides. 25(6):984–&.

Diettrich, J. Private comunication. British Antarctic Survey.

Espy, P. J. (2016). Private comunication.

Espy, P. J., Hibbins, R. E., Jones, G. O. L., Riggin, D. M., and Fritts, D. (2003). Rapid, large-scale temperature changes in the polar mesosphere and their relationship to meridional flows. 30(5).

Forbes, J. M. (1995). Tidal and Planetary waves. In Johnson, R. M. and Killeen, T. L., editors, *The Upper Mesosphere and Lower Thermosphere: A Review of Experiment and Theory*, volume 87 of *Geophys. Monogr. Ser.*, pages 67–87. AGU, Washington, D.C.

Forbes, J. M., Hagan, M. E., Miyahara, S., Vial, F., Manson, A. H., Meek, C. E., and Portnyagin, Y. I. (1995). Quasi 16-day oscillation in the mesosphere and lower thermosphere. 100:9149–9163.

French, W. J. R., Burns, G. B., and Espy, P. J. (2005). Anomalous winter hydroxyl temperatures at 69 degrees s during 2002 in a multiyear context. 32(12).

Fuller-Rowell, T. J. (1995). *The Dynamics of the Lower Thermosphere*, volume 87 of *Geophys. Monogr. Ser.*, pages 23–36. American Geophysical Union.

Gardner, C. S., Chu, X., Espy, P. J., Plane, J. M. C., Marsh, D. R., and Janches, D. (2011). Seasonal variations of the mesospheric fe layer at rothera, antarctica (67.5 degrees s, 68.0 degrees w). 116.

Geerts, B. and Linacre, E. (2016). Thermal wind. `http://www-das.uwyo.edu/~geerts/cwx/notes/chap12/thermal_wind.html`. [Online; accessed 15-March-2016].

Hedin, A. E., Fleming, E. L., Manson, A. H., Schmidlin, F. J., Avery, S. K., Clark, R. R., Franke, S. J., Fraser, G. J., Tsuda, T., Vial, F., and Vincent, R. A. (1996). Empirical wind model for the upper, middle and lower atmosphere. 58(13):1421–1447.

Hibbins, R. E., Shanklin, J. D., Espy, P. J., Jarvis, M. J., Riggin, D. M., Fritts, D. C., and Lubken, F. J. (2005). Seasonal variations in the horizontal wind structure from 0-100 km above Rothera station, Antarctica (67 degrees S, 68 degrees W). 5:2973–2980.

Hocking, W. (1999). Temperatures using radar-meteor decay times. *Geophysical Research Letters*, 26(21):3297–3300.

Hoffmann, C. (2012). *Application of CO as a tracer for dynamics in the polar winter middle atmosphere: A study based on ground-based microwave observations in Kiruna*. PhD thesis, Universität Bremen, Fachbereich fr Physik und Elektrotechnik, Institut fr Umweltphysik.

Kaiser, G. (1994). A friendly guide to wavelets.

Limpasuvan, V., Leovy, C. B., Orsolini, Y. J., and Boville, B. A. (2000). A numerical simulation of the two-day wave near the stratopause. *Journal of the Atmospheric Sciences*, 57(11):1702–1717.

Madden, R. A. (1979). Observations of large-scale traveling rossby waves. *Reviews of Geophysics*, 17(8):1935–1949.

Matsuno, T. (1970). Vertical propagation of stationary planetary waves in the winter northern hemisphere. *Journal of the Atmospheric Sciences*, 27(6):871–883.

Picone, J. M., Hedin, A. E., Drob, D. P., and Aikin, A. C. (2002). Nrlmsise-00 empirical model of the atmosphere: Statistical comparisons and scientific issues. 107(A12):1468.

Plumb, R. A. (1989). On the seasonal cycle of stratospheric planetary waves. *Pure and applied geophysics*, 130(2-3):233–242.

Prata, A. J. (1984). The 4-day wave. 41(1):150–155.

Rienecker, M. M., Suarez, M. J., Gelaro, R., Todling, R., Bacmeister, J., Liu, E., Bosilovich, M. G., Schubert, S. D., Takacs, L., G., K., Bloom, S., Chen, J., Collins, D., Conaty, A., da Silva, A., Gu, W., Joiner, J., Koster, R. D., Lucchesi, R., Molod, A., Owens, T., Pawson, S., Pegion, P., Redder, C. R., Reichle, R., Robertson, F. R., Ruddick, A. G., Sienkiewicz, M., and Woollen, J. (2011). MERRA: NASA's modern-era retrospective analysis for research and applications. *J. Climate*, 24:3624–3648.

Salby, M. L. (1981). Rossby normal modes in nonuniform background configurations. II. Equinox and solstice conditions. 38(9):1827 – 1840.

Salby, M. L. (1996). *Fundamentals of Atmospheric Physics*. Academic Press.

Straub, C., Espy, P. J., Hibbins, R. E., and Newnham, D. A. (2013). Mesospheric co above troll station, antarctica observed by a ground based microwave radiometer. *Earth System Science Data*, 5(1):199–208.

Stray, N. H. (2015). *Planetary waves in the northern MLT: Vertical coupling and effects*. PhD thesis, Norwegian University of Science and Technology, Faculty of Natural Sciences and Technology, Department of Physics.

Torrence, C. and Compo, G. P. (1998). A practical guide to wavelet analysis. *Bull. Amer. Meteor. Soc.*, 79:61–78.

Appendix

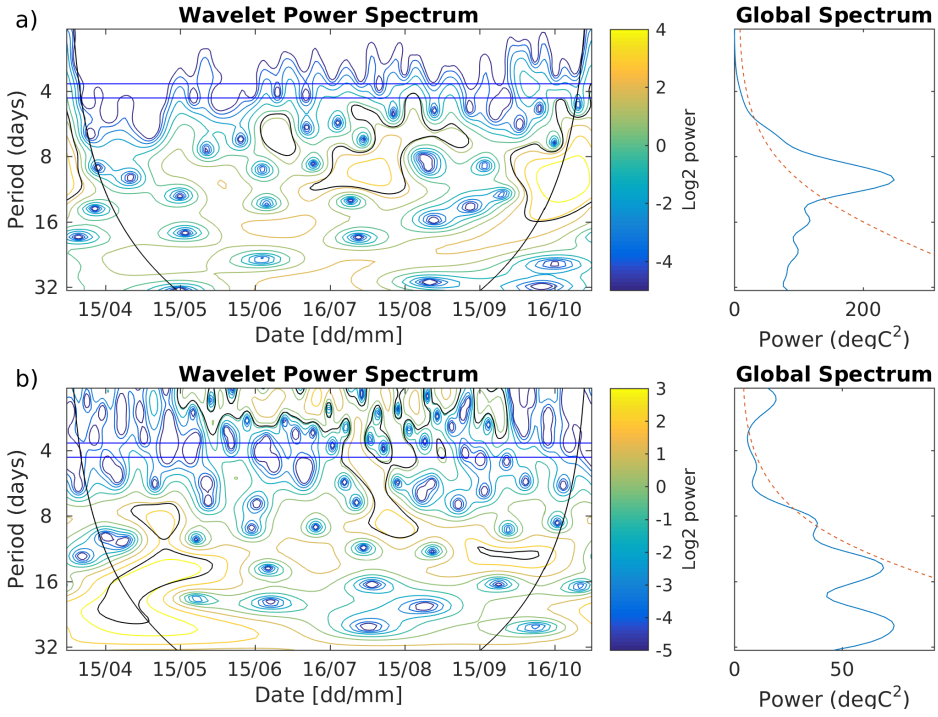

Figure 7.1: Wavelet analysis of the s2 wave for 2008 at a) 25 km altitude and b) 51 km. Each with the wavelet power spectrum on the left. The results outside the cone are subject to boundary effects. The black contour lines mark the significance level. On the right is the global spectrum with the significance level as dashed line. The horizontal lines mark the integration ranges for doppler shifted 4-day wave. See also tabel 4.1.

Nomenclature

Variables

a	radius of the earth
c	phase velocity
C_p	Specific heating rate per unit mass
f	Coriolis parameter $= 2\Omega \sin(\phi)$
g	gravity acceleration
H	scale hight $= \frac{RT}{g}$
k	zonal wave number
l	meridional wave number
m	vertical wave number
N	buoyancy frequency $= \sqrt{\kappa g / H}$
p	pressure
R	gas constant for dry air
t	time
T	Temperature
$\bar{u}$	zonal mean zonal wind
u	zonal wind
U_c	critical velocity
β	$= \frac{2\Omega \cos(\phi_0)}{a}$
κ	ratio of gas constant to specific heat at constant pressure $= \frac{R}{C_p} \approx \frac{2}{7}$
ρ	density
ϕ	Latitude
ψ'	geostrophic stream function
Ω	angular velocity of the earth $= 7.29 \times 10^{-5}\,\mathrm{s}^{-1}$

List of Abbreviations

BAS	British Antarctic Survey
CO	Carbon monoxide
GW	Gravity Wave
HWM	Horizontal Wind Model
MERRA	Modern Era Retrospective-Analysis
vmr	Volume mixing ratio
WACCM	Whole Atmospheric Community Climate Model

List of Figures

List of Tables